

<https://helda.helsinki.fi>

---

## Code-Free Development and Deployment of Deep Segmentation Models for Digital Pathology

Pettersen, Henrik Sahlin

2022-01-27

---

Pettersen , H S , Belevich , I , Royset , E S , Smistad , E , Simpson , M R , Jokitalo , E , Reinertsen , I , Bakke , I & Pedersen , A 2022 , ' Code-Free Development and Deployment of Deep Segmentation Models for Digital Pathology ' , Frontiers in Medicine , vol. 8 , 816281 . <https://doi.org/10.3389/fmed.2021.816281>

---

<http://hdl.handle.net/10138/341879>

<https://doi.org/10.3389/fmed.2021.816281>

---

cc\_by

publishedVersion

---

*Downloaded from Helda, University of Helsinki institutional repository.*

*This is an electronic reprint of the original article.*

*This reprint may differ from the original in pagination and typographic detail.*

*Please cite the original version.*



# Code-Free Development and Deployment of Deep Segmentation Models for Digital Pathology

Henrik Sahlin Pettersen<sup>1,2,3\*</sup>, Ilya Belevich<sup>4</sup>, Elin Synnøve Røyset<sup>1,2,3</sup>, Erik Smistad<sup>5,6</sup>, Melanie Rae Simpson<sup>7,8</sup>, Eija Jokitalo<sup>4</sup>, Ingerid Reinertsen<sup>5,6</sup>, Ingunn Bakke<sup>2,3</sup> and André Pedersen<sup>2,5,9</sup>

<sup>1</sup> Department of Pathology, St. Olavs Hospital, Trondheim University Hospital, Trondheim, Norway, <sup>2</sup> Department of Clinical and Molecular Medicine, Faculty of Medicine and Health Sciences, NTNU - Norwegian University of Science and Technology, Trondheim, Norway, <sup>3</sup> Clinic of Laboratory Medicine, St. Olavs Hospital, Trondheim University Hospital, Trondheim, Norway, <sup>4</sup> Electron Microscopy Unit, Institute of Biotechnology, Helsinki Institute of Life Science, University of Helsinki, Helsinki, Finland, <sup>5</sup> Department of Health Research, SINTEF Digital, Trondheim, Norway, <sup>6</sup> Department of Circulation and Medical Imaging, Faculty of Medicine and Health Sciences, NTNU - Norwegian University of Science and Technology, Trondheim, Norway, <sup>7</sup> Department of Public Health and Nursing, Faculty of Medicine and Health Sciences, NTNU - Norwegian University of Science and Technology, Trondheim, Norway, <sup>8</sup> The Clinical Research Unit for Central Norway, Trondheim, Norway, <sup>9</sup> The Cancer Foundation, St. Olavs Hospital, Trondheim University Hospital, Trondheim, Norway

## OPEN ACCESS

### Edited by:

Xin Qi,  
Eisai, United States

### Reviewed by:

António Polónia,  
Universidade do Porto, Portugal  
Guotai Wang,  
University of Electronic Science and  
Technology of China, China

### \*Correspondence:

Henrik Sahlin Pettersen  
henrik.s.pettersen@ntnu.no

### Specialty section:

This article was submitted to  
Pathology,  
a section of the journal  
Frontiers in Medicine

**Received:** 16 November 2021

**Accepted:** 24 December 2021

**Published:** 27 January 2022

### Citation:

Pettersen HS, Belevich I, Røyset ES, Smistad E, Simpson MR, Jokitalo E, Reinertsen I, Bakke I and Pedersen A (2022) Code-Free Development and Deployment of Deep Segmentation Models for Digital Pathology. *Front. Med.* 8:816281. doi: 10.3389/fmed.2021.816281

Application of deep learning on histopathological whole slide images (WSIs) holds promise of improving diagnostic efficiency and reproducibility but is largely dependent on the ability to write computer code or purchase commercial solutions. We present a code-free pipeline utilizing free-to-use, open-source software (QuPath, DeepMIB, and FastPathology) for creating and deploying deep learning-based segmentation models for computational pathology. We demonstrate the pipeline on a use case of separating epithelium from stroma in colonic mucosa. A dataset of 251 annotated WSIs, comprising 140 hematoxylin-eosin (HE)-stained and 111 CD3 immunostained colon biopsy WSIs, were developed through active learning using the pipeline. On a hold-out test set of 36 HE and 21 CD3-stained WSIs a mean intersection over union score of 95.5 and 95.3% was achieved on epithelium segmentation. We demonstrate pathologist-level segmentation accuracy and clinical acceptable runtime performance and show that pathologists without programming experience can create near state-of-the-art segmentation solutions for histopathological WSIs using only free-to-use software. The study further demonstrates the strength of open-source solutions in its ability to create generalizable, open pipelines, of which trained models and predictions can seamlessly be exported in open formats and thereby used in external solutions. All scripts, trained models, a video tutorial, and the full dataset of 251 WSIs with ~31 k epithelium annotations are made openly available at <https://github.com/andrepd/NoCodeSeg> to accelerate research in the field.

**Keywords:** computational pathology, deep learning, code-free, semantic segmentation, U-Net, open datasets, inflammatory bowel disease, colon

## INTRODUCTION

Visual evaluation of histopathological whole slide images (WSIs) is the gold standard for diagnosing an array of medical conditions ranging from cancer subtyping and staging to inflammatory and infectious diseases. The increasing shortage of pathologists, in combination with continually increasing biopsy load and lack of reproducibility for several common diagnoses between pathologists, calls for the application of novel methods to improve both diagnostic efficiency and reproducibility (1–5). Application of deep learning-based methods to histopathological WSIs holds promise of improving diagnostic efficiency and reproducibility, but is largely dependent on the ability to write computer code or buy commercial solutions. The introduction of large-scale digitization of histopathological WSIs has moved several pathology departments away from manual microscopy diagnostics to diagnosing digitized WSIs on computer screens (6). The successful application of deep learning-based classification and segmentation of WSIs holds great promise for a continually increasing introduction of computer assisted diagnostics for pathologists, possibly alleviating both pathologist workload and increasing reproducibility (7, 8). Many current solutions are either commercial software with limited transparency of the applied algorithms, limited export/import capability for other software, and limited availability for diagnostic departments with strained budgets. Existing commercial solutions include software such as Visiopharm,<sup>1</sup> Halo AI,<sup>2</sup> and Aiforia,<sup>3</sup> but also, open-source alternatives such as MONAI-Label,<sup>4</sup> H-AI-L, QuickAnnotator (9–12), and ZeroCostDL4Mic (12). These open-source solutions, however, either lack a full annotation, training and visualization pipeline, require some degree of programming experience, or use commercial servers. This calls for the development and use of open-source solutions that enable transparency of the image analysis pipelines, the possibility of exporting and importing results and data between applications and use of local data without the requirement of uploading restricted images to commercial servers.

The open-source software QuPath is a user-friendly solution for WSI analysis (13). Its tools offer means for tumor identification and biomarker evaluation using conventional non-deep learning-based machine learning methods with possibilities of batch-processing and scripting, as well as communication with auxiliary image analysis applications such as ImageJ. However, no deep learning-based image segmentation functionality exists for QuPath to date, except for the possibility of calling the StarDist nucleus segmentation method (14) from a customizable script in the latest 0.3.x release.

Application of deep learning approaches to biological imaging during recent years has significantly boosted our capabilities to segment structures of interest from collected images and

make them ready for visualization and quantitative analysis (15). Despite the potential quality of generated results, use of deep learning in routine research projects is still quite limited. This limitation is mostly due to a relatively high threshold barrier that is hard to overcome by researchers without extensive knowledge of computer science and programming experience. The typical deep learning workflows require knowledge of deep learning architectures, Python programming abilities, and general experience with multiple software installations. The code-free solution DeepMIB was published to help with all these aspects and with a hope to make deep learning available to a wider community of biological researchers (16). DeepMIB is a user-friendly software package that was designed to provide a smooth experience for training of convolutional neural networks (CNN) for segmentation of light and electron microscopy datasets. It is suitable for anyone with only very basic knowledge of deep learning and does not require computer programming skills.

DeepMIB comes bundled with Microscopy Image Browser (17), which is a free, open-source software package for image processing, segmentation, and quantification of microscopy datasets. Both packages are written with MATLAB, they are easy to install, and can be used either under the MATLAB environment or as a stand-alone application on Windows, macOS, or Linux.

Image segmentation in DeepMIB is organized as a step-by-step workflow, which starts with selection of a CNN architecture [2D or 3D, U-Net (18) or SegNet (19)], and definition of the most central training hyperparameters. The provided architectures are efficient and are shown to generate generalizable models even with sparse training data (20). To extend the training base, DeepMIB comes with multiple (19 for 2D, and five for 3D) augmentation filters that can be individually configured, previewed, and tuned to fulfill the needs of a specific project. The resulting CNN models can be used to predict images directly in DeepMIB or be exported to ONNX format. DeepMIB further provides the ability to test the performance of the trained model on an unseen test set with ground truth labels and evaluate the network performance using multiple metrics, such as accuracy (ACC), dice similarity coefficient (DSC) and intersection over union (IoU). The MIB software is openly available on GitHub.<sup>5</sup>

Multiple studies propose deep learning solutions for computational pathology (8). However, only some make their trained models openly available; even if they were, using them generally requires programming experience. In digital pathology, this is especially challenging due to the large image sizes of up to 200,000 × 100,000 color pixels, which makes it computationally demanding to deploy models and visualize the predictions with the WSI. Although MIB is able to run inference on the WSI level, the browser is not suitable for displaying such large images, only supports semantic segmentation models, and does not have a streamlined algorithm to exclude prediction on background glass areas. This slows viewing speed, versatility, and prediction runtime. FastPathology (21) was developed to offer a user friendly direct WSI prediction viewer to pathologists. The software is free, open-source, and focused on high-performance

<sup>1</sup><https://visiopharm.com/visiopharm-digital-image-analysis-software-features/ai-features/>

<sup>2</sup><https://indicalab.com/halo-ai/>

<sup>3</sup><https://www.aiforia.com/>

<sup>4</sup><https://github.com/Project-MONAI/MONAIlabel/>

<sup>5</sup><https://github.com/Ajaxels/MIB2>

computing to minimize memory usage and runtime. The software is based on the C++ library FAST (22, 23).

FastPathology enables the user to deploy deep learning methods directly from the Graphical User Interface (GUI). The software includes a rapid, pyramidal viewer for visualizing WSIs and supports overlays of segmentations. New models can be imported without implementation, by defining a FAST text pipeline that contains information about the model and how it should be handled. The software supports various inference engines i.e., TensorRT, OpenVINO, and TensorFlow (24). TensorRT enables the fastest graphical processing unit (GPU) inference, whereas OpenVINO is among the fastest central processing unit (CPU) alternatives. The recommended format is ONNX, as both OpenVINO and TensorRT support it. FastPathology is openly available on GitHub,<sup>6</sup> including trained models and test data.

Here we present a pipeline for developing and deploying high performance deep segmentation models for WSIs using three software packages, each specialized in different parts of the workflow (Figure 1). QuPath is efficient for quick annotations of WSIs, DeepMIB provides capabilities for training CNNs without programming, and FastPathology for efficient inference and visualization of full resolution model predictions with the WSI. The proposed pipeline is demonstrated on a use case of segmentation of colon epithelium and is shown to produce models that perform at a clinical acceptable accuracy and runtime level.

## Example Application

The human gut mucosa comprises both non-immune and immune cells working together in a complex manner to maintain mucosal immunity. In lamina propria there are a broad range of different innate and adaptive immune cell subtypes that are separated from gut content and microbiota by a single layer of intestinal epithelial cells at the surface. These specialized epithelial cells have a pivotal role in producing mucus and antimicrobial factors, or immunomodulating cytokines involved in crosstalk between the different systems, in addition to being a physical barrier. Intermingled between the epithelial cells resides a population of intraepithelial T lymphocytes (IEL), many of which are unconventional T cells. These cells have the characteristics of both innate and adaptive immunity, and they can move and surveil the epithelium. This makes them able to respond rapidly and diverse as an effective first line defense against microbe invasion in addition to being important for maintenance of mucosal homeostasis (25, 26). Dysregulation of IELs is generally correlated to loss of mucosal barrier integrity and is implicated in the pathogenesis of several gut disorders like infections with bacteria, parasites and viruses, inflammatory processes like inflammatory bowel disease, lymphocytic colitis, and celiac disease, and possibly also tumor development (25). A lot is still unknown about the functions and clinical significance of the different IEL subtypes, and more research is needed (25, 27). Tools that provide objective and reproducible quantitative

data from tissue sections will open new doors in research and allow for new questions to be posed.

For inflammatory disorders of the GI tract that involves numerical definitions, like celiac disease or lymphocytic colitis, quantification of IEL is part of the pathologist's job. This can be done by roughly giving a visual estimate, or by manual counting of smaller areas and then make a global estimate based on that. Looking at tissue sections, the eyes are more easily drawn to the areas with the highest densities and could possibly lead to an overestimation of the number of IELs. A tool for epithelium segmentation that enables automated quantification of IELs could serve as a calibration instrument for pathologists. It can save pathologists from spending time and energy on something that can be done much more objectively by a machine. It can be of great value in research on the epithelial immune microenvironment in inflammatory and neoplastic disorders. In the present study, we have included both HE and CD3 stained images to demonstrate the potential use of this technique both for quantifying different populations of intraepithelial immune cells with the help of immunostaining and the potential (by further annotation and training) to quantify e.g., intraepithelial granulocytes directly on HE stained images. Quantification of CD3 immunostained IELs after epithelial segmentation can be achieved with high accuracy in QuPath, but is not demonstrated as part of this publication. Further developing deep learning-based models for segmentation of other important mucosal structures (e.g., lymphoid aggregates, basal plasmacytosis, specific cell types, tumors), and for other types of immunohistochemical evaluations to integrate information of protein expression, cell types and tissue structure, would vastly expand the value of this tool for research and in diagnostics.

Here, we demonstrate a use case of automatic, deep learning-based segmentation of colon epithelium with no requirements for computer programming. We further publish the resulting near pixel accurate dataset of epithelium segmentation of 140 HE stained WSIs and 111 CD3 immunostained WSIs from colon biopsies of both healthy controls and patients with active inflammatory bowel disease.

## MATERIALS AND METHODS

### Dataset of Endoscopic Colon Biopsies

Formalin fixed paraffin embedded (FFPE) biopsies of colonic mucosa were extracted from the NTNU/St. Olavs hospital, Trondheim University Hospital (Norway) biobank of patients with confirmed inflammatory bowel disease or healthy controls with gastrointestinal symptoms but no macroscopic- or microscopic disease. Inclusion and colonoscopies were performed at the Department of Gastroenterology and Hepatology at St. Olavs hospital, Trondheim University Hospital from 2007 to 2018. All patients gave written informed consent and ethical approvals were obtained from the Central Norway Regional Committee for Medical and Health Research Ethics (reference number 2013/212/REKMidt). Consent to publish the anonymized WSI dataset was given by REKMidt in 2021. Each database ID-number used in this

<sup>6</sup><https://github.com/AICAN-Research/FAST-Pathology>

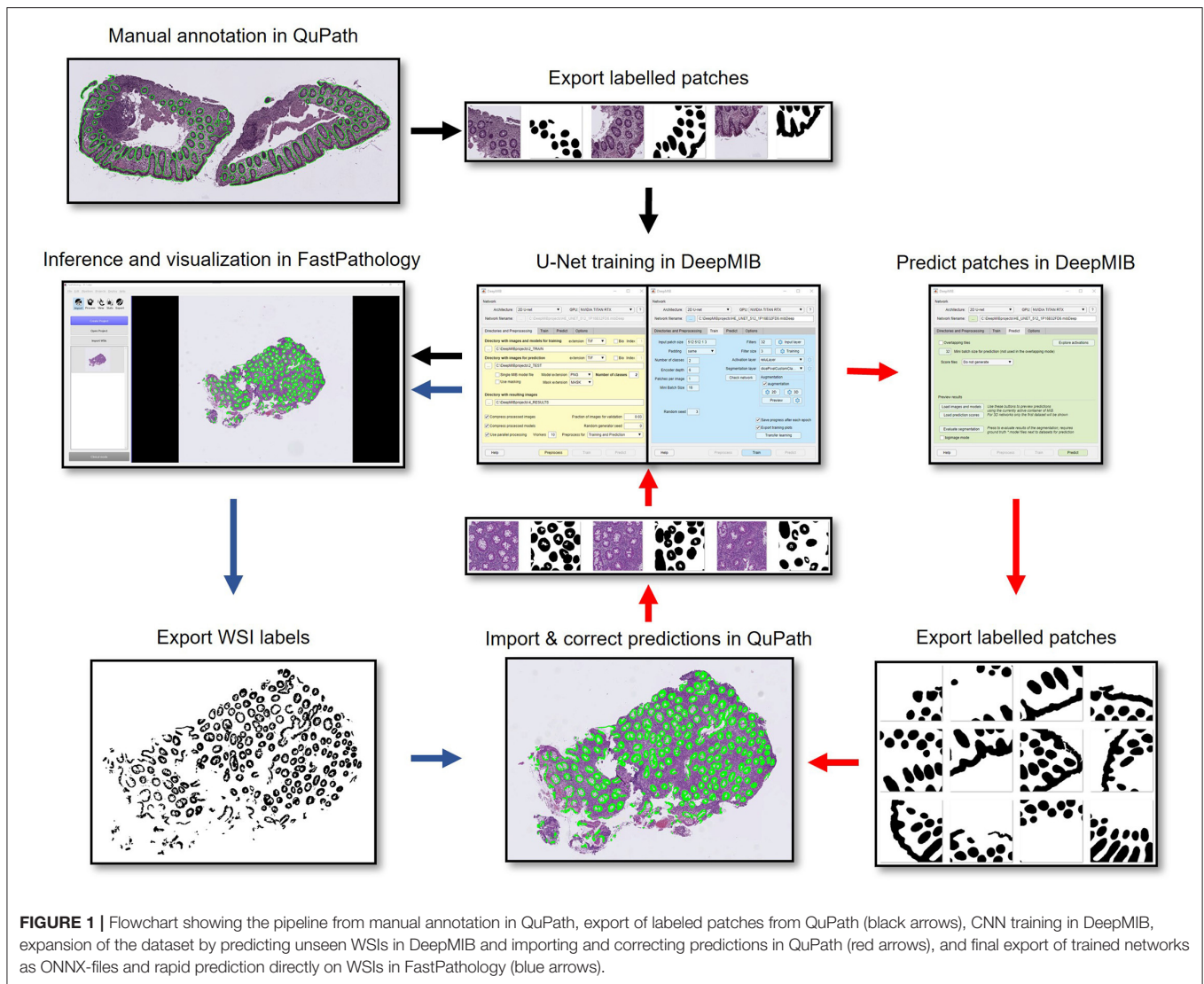


**FIGURE 1** | Flowchart showing the pipeline from manual annotation in QuPath, export of labeled patches from QuPath (black arrows), CNN training in DeepMIB, expansion of the dataset by predicting unseen WSIs in DeepMIB and importing and correcting predictions in QuPath (red arrows), and final export of trained networks as ONNX-files and rapid prediction directly on WSIs in FastPathology (blue arrows).

study was changed to new anonymized IDs only containing the information “active” or “inactive” disease and whether the WSI has “HE” or “CD3” staining. The full dataset of 251 WSIs with ~31k epithelium annotations is made openly available at DataverseNO: <https://doi.org/10.18710/TLA01U> (28).

FFPE sections of 4 μm were cut, mounted on slides and either stained with hematoxylin (Mayer’s) and Eosin (Y) (HE) or subjected to standard pre-treatment with quenching of endogenous peroxidase and boiling in Tris EDTA pH9 for antigen retrieval before immunohistochemistry. Primary antibody for the T lymphocyte marker was mouse anti-human CD3 (M7254, clone F7.2.38, Dako Agilent, CA, USA), diluted 1:50 in antibody diluent Tris buffer with 0.025% Tween-20 and 1% BSA and incubated overnight at 4°C. Immunoreactions were visualized with the secondary antibody rabbit/mouse EnVision-HRP/DAB+ kit (K5007, Dako Agilent) and counterstaining with haematoxylin. Omission of the primary antibody was used as negative

control and sections from human peripheral lymph node as positive control.

### U-Net Based Epithelial Segmentation Using QuPath and DeepMIB

The HE and CD3 immunostained slides were scanned using a Hamamatsu NanoZoomer S360 (Hamamatsu Photonics, Japan) scanner at ×40 magnification. Slides were imported into the open-source image analysis software QuPath (13). Epithelium was annotated for ~30 out of 111 CD3 stained WSIs by an experienced gastrointestinal pathologist and checked and corrected by a second pathologist. To make the images compatible with efficient training of semantic segmentation neural networks in DeepMIB, 2,048 × 2,048 pixels image tiles were exported as 4× downsampled files (from 2,048 × 2,048 pixels with 512 pixels overlap to a downsampled size of 512 × 512 pixels with 128 pixels overlap) with corresponding binary mask labels (\*.png) from QuPath. Overlapping tiles were used to avoid inference errors at the edges of the patches when

importing labels back into QuPath. WSIs often contain 50–90% white background, which will make the exterior class completely dominant in training. Therefore, a glass detection method was used, similarly as done in a previous study (21), and patches with <25% tissue were discarded.

Images and labels were split randomly into an 80/20% train/test split at the WSI level, such that only unseen WSIs were present in the test set. The data was then placed in separate train and test folders, each containing separate “Images” and “Labels” sub-folders.

Two semantic segmentation neural networks were used in this paper: U-Net (18) and SegNet (19). U-Net is a fully-convolutional encoder-decoder neural network initially developed for the purpose of biomedical image segmentation. U-Net is one of two available 2D semantic segmentation networks in DeepMIB which allows optimization of hyperparameters such as U-Net depth, number of filters and input patch size for each segmentation task (16). SegNet is a fully-convolutional encoder-decoder neural network where the encoder part is identical to the 13 convolutional layers in the much-used VGG16 network (19).

A SegNet network with depth of 6 layers with 32 initial filter and input patch size of  $256 \times 256$  pixels was trained until validation loss stagnation around 5% in DeepMIB (MATLAB version 2021a, MIB version 2.8, CUDA version 11.3). The trained SegNet was then used to predict the remaining  $\sim 70$  WSIs by exporting  $4 \times$  downsampled  $512 \times 512$  image patches with 128 pixels overlap from QuPath. Patches containing <25% tissue were deleted. The resultant images with predicted label files were then loaded in DeepMIB for evaluation and the label patches saved as TIF files. The TIF files were then imported back into QuPath as annotations. Annotations were then confirmed, and errors were manually corrected in QuPath by a pathologist for the remaining WSIs to achieve a dataset of 111 WSIs. A final refinement of the dataset was done by predicting the full dataset and correcting in DeepMIB. The  $\sim 5\%$  patches with the lowest mean IoU scores as evaluated inside DeepMIB were exported as text-file lists and the patches could then be copied to a different folder using a Windows PowerShell script (all scripts used in this paper is made available in the NoCodeSeg GitHub repository). The worst performing image patches and their corresponding labels were then loaded and corrected in DeepMIB. A similar strategy was applied to the HE-stained dataset of 140 WSIs, using the U-Net trained on CD3 immunostained WSIs to predict and correct an initial batch of  $\sim 30$  HE-stained WSIs. Then training a U-Net on the initial batch of annotated HE-stained WSIs, applying it on the remaining HE-stained WSIs, and retraining the U-Net. The final datasets (140 HE-stained and 111 CD3 immunostained WSIs, or 6322 HE and 4323 CD3  $4 \times$  downsampled  $512 \times 512$  image patches in each dataset) were again split into an 80/20% train/test split at the WSI level, such that 36 (HE) and 21 (CD3) previously unseen WSIs were present in the test set and new networks were trained from scratch using DeepMIB to assess the performance of the software on this larger train/test set (see **Table 1**).

Finally, two CNNs, SegNet and U-Net, were then trained using DeepMIB. To achieve maximum variety of different image patches per mini batch, the number of patches DeepMIB extracts

per image in a single mini batch was set to one. Initially the number of patches per image was set to the same number as the number of applied augmentations, however, this produced inferior results to using just one patch per image per mini batch. Three percent of the training set images were randomly chosen by DeepMIB for the validation set. A fixed random generator seed was used to make comparison between training different conditions more direct. Several hyperparameters were tested, such as variable input patch size ( $128 \times 128$ ,  $256 \times 256$ ,  $512 \times 512$ ), number of filters (16, 24, 32, 64), network depth (4, 5, 6, 7, 8), and the presence and absence of augmentations. Finally, U-Net and SegNet were trained for 200 epochs, which was the number of epochs required for training loss stagnation. Further global training settings were as follows: Padding: Same; Solver: Adam; Shuffle: Every-epoch; Initial learning rate: 0.00005; L2 Regularization: 0.0001; Decay rate of gradient moving average: 0.9; Decay rate of squared gradient moving average: 0.999. Augmentations used in all described trainings were performed in a blended fashion (MIB version 2.8) with a 30% probability for each augmentation to be applied to each augmented image patch during training. The fraction of images for augmentation was set to 75%, i.e., 25% of input image patches were not augmented, while 75% had a 30% chance of being augmented with either of the following augmentations [numeric limits show in brackets]: Random left-right/top-bottom reflections, random 90/270-degree rotations, random X/Y/X+Y image scaling [1.0, 1.1], random color augmentation: Hue [−0.03, 0.03], saturation [−0.05, 0.05], random intensity augmentation: brightness [−0.1, 0.1], contrast [0.9, 1.1], and zero-mean Gaussian blur with standard deviation in range [0, 0.5] (see **Supplementary Figures 1, 2**).

A selection of metrics was extracted for each patch from DeepMIB, and metrics were then averaged at the WSI-level (**Table 1**). The reported metrics were produced from calculating the WSI-level average. The following metrics were calculated: micro and macro-averaged pixel-wise accuracy, macro and weighted IoU, and class-wise DSC for the exterior Epithelium classes. U-Net proved to consistently outperform SegNet for both the HE and CD3 dataset (see **Table 1**). Initially, increasing input patch sizes were tested, with size  $64 \times 64$ ,  $128 \times 128$ ,  $256 \times 256$ , and  $512 \times 512$ . The available 24 GB GPU allowed a maximum batch size of 16 for a U-Net with  $512 \times 512$  patch size, 32 filter, and depth of 6. Thus, these settings (16 batch size, 32 filter, depth 6) were kept for all the different input patch size trainings to be comparable.

## Deployment in FastPathology

The best performing trained U-Net model from DeepMIB was exported to the ONNX format using the ExportONNXNetwork method from the Deep Learning Toolbox in MATLAB. As ONNX does not currently support MATLAB's implementation of the UnPooling operation in SegNet, U-Net was the only model converted to ONNX.

We defined an inference pipeline consisting of applying the trained segmentation model across the WSI in an overlapping, sliding window fashion, similarly as done in a previous study (21). The result of each patch was binarized using a threshold

**TABLE 1** | Comparative accuracies on the HE stained ( $n = 36$ ) and CD3 immunostained ( $n = 21$ ) test sets with different hyperparameter settings for U-Net and SegNet.

Stain	Arch.	Patch size	Nr. of filt.	Depth	Batch size	MICRO Acc	MACRO Acc	MACRO IoU	Weig. IoU	Ext. DSC	Epith. DSC
HE	U-Net	512 × 512	32	6	16	<b>0.989</b>	0.972	<b>0.955</b>	<b>0.978</b>	<b>0.992</b>	<b>0.953</b>
HE	U-Net	256 × 256	32	6	16	<b>0.989</b>	<b>0.983</b>	0.938	<b>0.978</b>	<b>0.992</b>	0.920
HE	U-Net	256 × 256	32	6	32	0.988	0.978	0.936*	0.976	0.991	0.920
HE	U-Net	256 × 256	64	6	32	0.987	0.974	0.935*	0.975	0.991	0.919
HE	U-Net	128 × 128	32	6	16	0.988	<b>0.983</b>	0.932*	0.977	0.991	0.911
HE	U-Net	64 × 64	32	6	16	0.985	0.965	0.924*	0.971	0.989	0.904
HE	SegNet	512 × 512	32	6	16	0.983	0.964	0.928*	0.967	0.988	0.918
HE	SegNet	256 × 256	32	6	16	0.987	0.973	0.939*	0.974	0.991	0.927
HE	SegNet	128 × 128	32	6	16	0.979	0.964	0.904*	0.960	0.985	0.884
CD3	U-Net	512 × 512	32	6	16	<b>0.990</b>	<b>0.981</b>	<b>0.955</b>	<b>0.980</b>	<b>0.992</b>	<b>0.948</b>
CD3	U-Net	256 × 256	32	6	16	0.987	0.977	0.931*	0.974	0.990	0.911
CD3	SegNet	512 × 512	32	6	16	0.976	0.953	0.920*	0.954	0.983	0.919
CD3	SegNet	256 × 256	32	6	16	0.971	0.949	0.898*	0.945	0.979	0.889

All metrics were reported as the mean at WSI-level. Best performing methods are highlighted in bold, for each respective metric and for each data set. The number of train/validation/test patches for each dataset was as follows: HE: (4973/154/1195); CD3 (3539/110/674). Stars indicate significant differences ( $p < 0.01$ ) compared to the single best performing architecture within each dataset (HE and CD3 U-Net 512x512, 32 filters, 16 batch, respectively) using a two-level mixed regression model (see **Supplementary Table 1**). ARCH, Architecture; FILT, Filters; NR, Number; ACC, Accuracy; WEIG, Weighted; EXT, Exterior; IOU, Intersection over Union; DSC, Dice Similarity Coefficient; EPITH, Epithelial; HE, Hematoxylin-Eosin; CD3, T-cell lymphocyte immunomarker.

of 0.5, before being stitched to form a tiled, pyramidal image. When inference was complete, the resulting pyramidal image was exported to the disk in the open TIFF format.

To demonstrate the performance of FastPathology, runtime experiments were conducted. Runtimes were measured for the total inference pipeline, as well as for individual pipeline components (runtimes reported are without overlapping inference). The experiments were repeated ten times for the same WSI, using three different inference engines (OpenVINO CPU, OpenVINO GPU, and TensorRT). For each metric, the average of the ten runs were reported. The source code to reproduce the experiments can be found on GitHub<sup>7</sup>.

### Computer Hardware

Runtime experiments were performed on a Razer Blade 15 Base laptop, with an Intel i7-10750H CPU @ 2.60 GHz, 32 GB RAM, an Intel UHD graphics integrated GPU, and NVIDIA RTX 2070 Max-Q (8 GB) dedicated GPU. All other analyses were performed on a Dell Precision 5820 Tower, with an Intel(R) Xeon(R) W-2155 CPU @ 3.30GHz, 96 GB RAM, and a NVIDIA Titan RTX (24 GB) dedicated GPU.

### Statistical Methods

For the statistical analyses in **Table 1**; **Supplementary Table 1**, the mean IoU for each neural network architecture, for the HE and CD3 datasets separately, was compared to the best performing architecture (HE/CD3 U-Net 512 × 512, 32 filters, 16 batch). Between-architecture comparisons were performed using a two-level linear mixed regression model, where architectures were specified as level 1, image patches as level 2 and with robust variance estimates clustered by WSI and a random intercept for patch. Analyses were performed using Stata/MP 16.1 (College

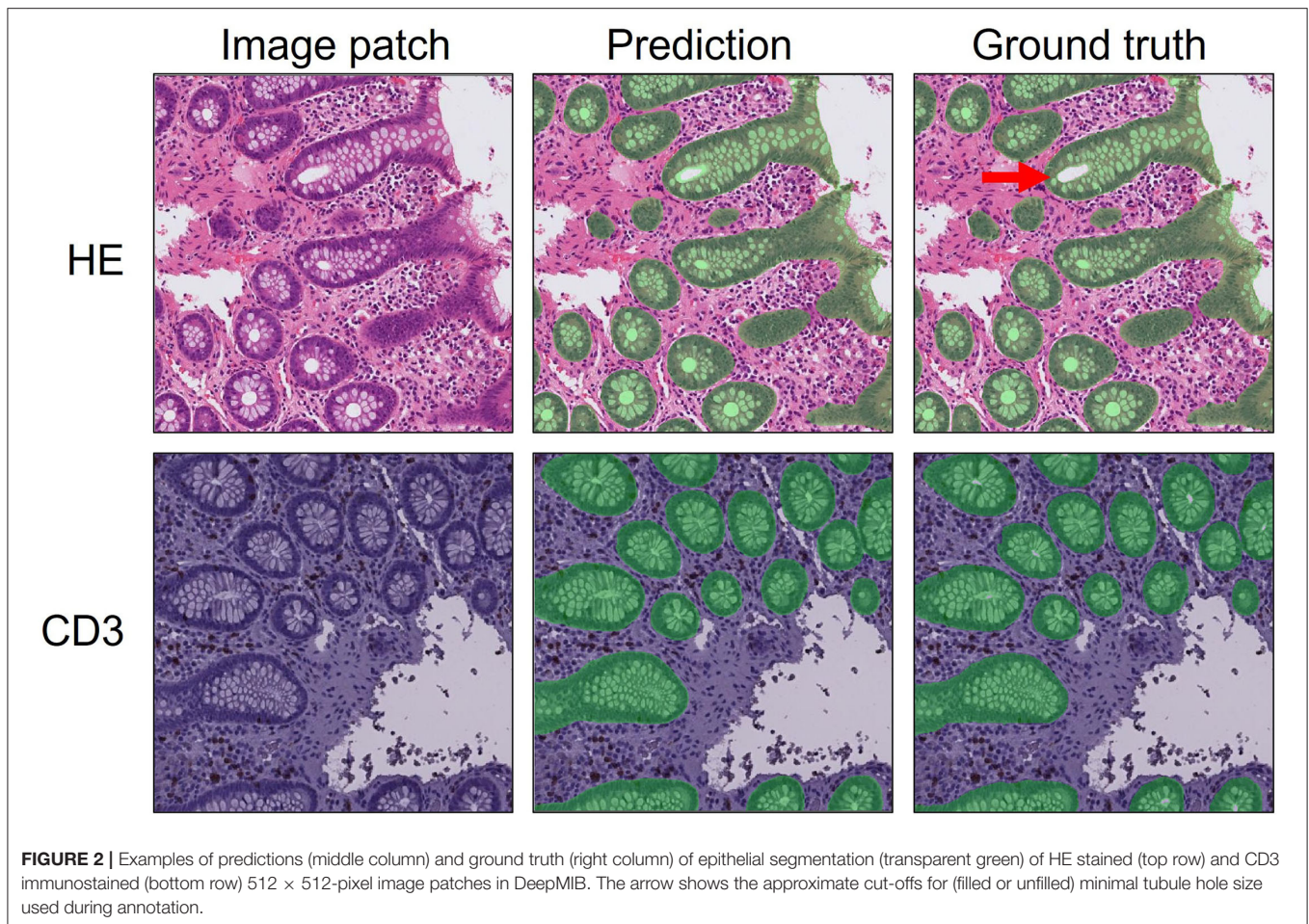
Station, Texas) and the estimated mean difference is presented together with 95% CI and  $p$ -values without correction for multiple comparisons.

## RESULTS

### Annotation of Colon Epithelium Through Active Learning Using QuPath and DeepMIB

We performed several trainings in DeepMIB using two different CNNs (i.e., SegNet and U-Net), with a variety of hyperparameters to find the highest performance (see section U-Net Based Epithelial Segmentation Using QuPath and DeepMIB). Initially a SegNet network was trained and applied to new unannotated WSIs. Annotations were imported and manually corrected in QuPath by a pathologist. Subsequent training cycles were performed with U-Net 512 × 512 in a repetitive fashion described in **Figure 1** (DeepMIB training, inference of new WSIs and import into QuPath for correction of annotations, export for new DeepMIB training, etc.) to achieve a final dataset of 111 WSIs (see **Figure 1**). A final refinement of the annotations was done by exporting individual accuracy scores for all image patches exported from DeepMIB. This allowed sorting of the patches which was in most disagreement with the U-Net predictions (typically mean IoU scores below 0.85). The set of ~5% worst performing patches were then loaded in DeepMIB such that a pathologist could refine the annotations directly on several hundred image patches instead of going through the whole dataset of ~5,000–7,000 image patches. This final refinement made it possible to achieve almost pixel accurate epithelial segmentation of ~100 WSIs. The top-performing CD3-trained network was used to repeatedly predict and correct

<sup>7</sup><https://github.com/andrepd/NoCodeSeg>



the 140 HE stained WSIs, following the workflow described in **Figure 1**.

### Training of Deep Semantic Segmentation of Colon Epithelium Using DeepMIB

This resulted in a final dataset of fully annotated patches, from 140 HE stained and 111 CD3 immunostained colon biopsy WSIs (see **Figure 2** for examples). The datasets were split into the two subsets: train (80%;  $n = 104$  HE;  $n = 90$  CD3) and test set (20%;  $n = 36$  HE;  $n = 21$  CD3). Two segmentation networks (i.e., U-Net and SegNet) were then trained on the final refined datasets to assess performance. We limited each training to 200 epochs and a similar global training setting (see section Materials and Methods) for comparable results (see **Table 1**). A step-by-step tutorial video demonstrating the full pipeline and for setting training hyperparameters in DeepMIB has been made available online (<https://youtu.be/9dTfUwnL6zY>).

For the U-Net models on the HE dataset, an increase in segmentation accuracy was observed with increasing input patch sizes from  $64 \times 64$  (Epithelium DSC 0.904) to  $512 \times 512$  (Epithelium DSC 0.953). This segmentation accuracy decline was statistically significant for all comparisons to the HE U-Net  $512 \times 512$ , except for HE U-Net  $256 \times 256$

with the same number for filters (32) and batch size (16) (see **Table 1**; **Supplementary Table 1**). The best segmentation accuracy for SegNet was observed with input patch size  $256 \times 256$  for the HE dataset (Epithelium DSC 0.927). For the CD3 dataset, the maximum segmentation accuracy was observed for  $512 \times 512$  input patches for both U-Net and SegNet (Epithelium DSC of 0.948 and 0.919, respectively), and as was the case for the HE dataset, the larger patch input CD3 U-Net  $512 \times 512$  performed significantly better than all the other CD3 trained architectures (see **Table 1**; **Supplementary Table 1**).

There was a negligible difference in segmentation accuracy when increasing the number of filters from 32 to 64 (Epithelium DSC 0.920 vs. 0.919) or increasing the batch size from 16 to 32 (Epithelium DSC 0.920 vs. 0.920). U-Net consistently and statistically significantly outperformed SegNet (see **Table 1**; **Supplementary Table 1**). U-Net's top segmentation accuracies of Epithelium DSC of 0.953 and 0.948 (HE and CD3, U-Net  $512 \times 512$ ), were significantly better than the top performing SegNet models with Epithelium DSCs of 0.927 and 0.919 (HE SegNet  $256 \times 256$  and CD3 SegNet  $512 \times 512$ ). Further testing with different depth of the networks was also performed, but depth 6 seemed to perform consistently higher (data not shown).



**TABLE 2** | Runtime measurements of different inference engines using FastPathology.

Inference engine	Processor	Patchgen. (ms)	NN input (ms)	NN inference (ms)	NN output (ms)	Patch sticher (ms)	Export wsi tiff (ms)	Total time/wsi (s)
OpenVINO CPU	Intel i7-10750H	3.65	1.03	135.31	0.80	2.76	7.09	76.38
OpenVINO GPU	Intel UHD graphics	<b>3.29</b>	1.26	133.96	1.25	3.46	7.83	76.65
TensorRT	RTX 2070 Max-Q	5.12	<b>0.80</b>	<b>7.31</b>	<b>0.19</b>	<b>1.35</b>	<b>5.40</b>	<b>5.60</b>

The table shows means of 10 runtime experiments for the  $256 \times 256$  pixel input patch size U-Net applied to a single representative WSI from the dataset (540 patches without overlap). Inference measurements show runtime per  $256 \times 256$  patch in milliseconds (ms). Export of a full WSI pyramidal TIFF performed once after inference is reported in ms, and the total runtime for the full WSI (including TIFF export) is shown in seconds (s). The fastest runtimes are highlighted in bold. GEN, Generator; NN, Neural Network; WSI, Whole Slide Image.

Using our best performing  $256 \times 256$  U-Net model, the proposed inference pipeline took  $\sim 5.60$  s to complete for the entire WSI using FastPathology (see **Table 2**). In our experience, this is well within the range for running direct inference in a clinical setting, and even the longest CPU-based inference times would be unlikely to limit the use of such algorithms by pathologists. The fastest inference engine was TensorRT, whereas using OpenVINO took  $\sim 76.5$  s (a  $13.7\times$  improvement using TensorRT). The main bottleneck of the pipeline was the neural network inference. For OpenVINO,  $\sim 94.3\%$  of the patch runtime was due to inference alone, whereas for TensorRT this was only  $\sim 49.5\%$ . Using TensorRT, our inference pipeline required  $\sim 2.1$  GB of VRAM and  $\sim 4.2$  GB of RAM for running inference on a full WSI with a network trained with patch sizes of  $256 \times 256$  pixels.

## DISCUSSION

### Benefits and Limitations With Using Multiple Software Solutions

The motivation of this study was to segment epithelium in a large dataset from a biobank of normal and diseased (inflammatory bowel disease) colon biopsies. We aimed to achieve this without the need for computer coding abilities, while simultaneously taking advantage of the strongest sides of available open-source software solutions. We demonstrate an open-source, free-to-use pipeline that can achieve high accuracy segmentation of histopathological WSIs available to a broad user base without the ability to write computer code. We further demonstrate the advantages of using open-source, non-proprietary software and formats that can be exchanged between these three software packages. The pipeline could be improved by incorporating all tasks into a single software solution. However, the use of several software solutions and exchange of information between them makes it possible to use more specialized open-source solutions best suited for each task—QuPath for annotations of whole slide images, DeepMIB for neural network training, and FastPathology for efficient inference and visualization of trained models. A disadvantage of such a multi-software pipeline is that it requires three separate software installations, which over time might diverge in compatibility and use different versions of auxiliary software, such as versions of CUDA.

Even though the pipeline does not require the ability to write computer code, it does require the use of some scripts, such as the

QuPath export/import scripts. This requires copy/pasting of pre-existing code, with any relevant changes to the parameters within those scripts to make the pipeline suitable for different tasks. In the near future, it is likely that this will be possible solely through the GUI in QuPath.

The epithelial segmentation accuracy was comparably high for both the best performing U-Nets on HE (DSC Epithelium 0.953) and CD3 images (DSC Epithelium 0.948), demonstrating the robustness of U-Net for this task. Segmentation accuracy was generally better with larger patch sizes ( $512 \times 512$  vs.  $256 \times 256$  DSC Epithelium 0.953 vs. 0.920), however  $256 \times 256$  patch size networks require much less GPU memory for training and inference. There was a statistically significant difference between the best performing architectures (HE/CD3 U-Net  $512 \times 512$ , 32 filters, 16 batch) compared to each of the other architectures in both datasets (HE and CD3). These statistically significant differences, should not, however, be automatically perceived as clinically significant different segmentation performance. Although statistically significant, the differences in mean IoU/epithelium DSC between the top performing architectures were small and may not result in clinically perceivable differences. Application of the segmentation models for downstream quantitative purposes (e.g., the number of intraepithelial lymphocytes) may more accurately address the cut-off for clinically significant performance of such models in future studies. We have not compared the segmentation accuracy of our trained models to current state-of-the-art architectures (29, 30). However, DSC scores for the epithelial class up to  $\sim 95\%$  on unseen test sets show little room for considerable improvement, making the U-Net segmentation accuracy for these data sets probably near state-of-the-art. It has also been argued by others (31), that there is little to gain from changing neural network architecture for semantic segmentation. The U-Net architecture presented can also easily be tuned code-free to be better suited for a specific task. The datasets are published with this paper and comparison to state-of-the-art models will therefore be possible by others.

### The Dataset and Annotations

Several issues arose during annotation. Defining a pixel-accurate epithelium ground truth is difficult as several images contain artifacts (folds, blurred areas, poorly fixated tissue, stain exudates, etc.) as well as intraepithelial inclusions (e.g., granulocytes) (see **Figure 3**). These cannot be easily defined into the dichotomous categories: epithelium or exterior, as e.g., folded tissue might

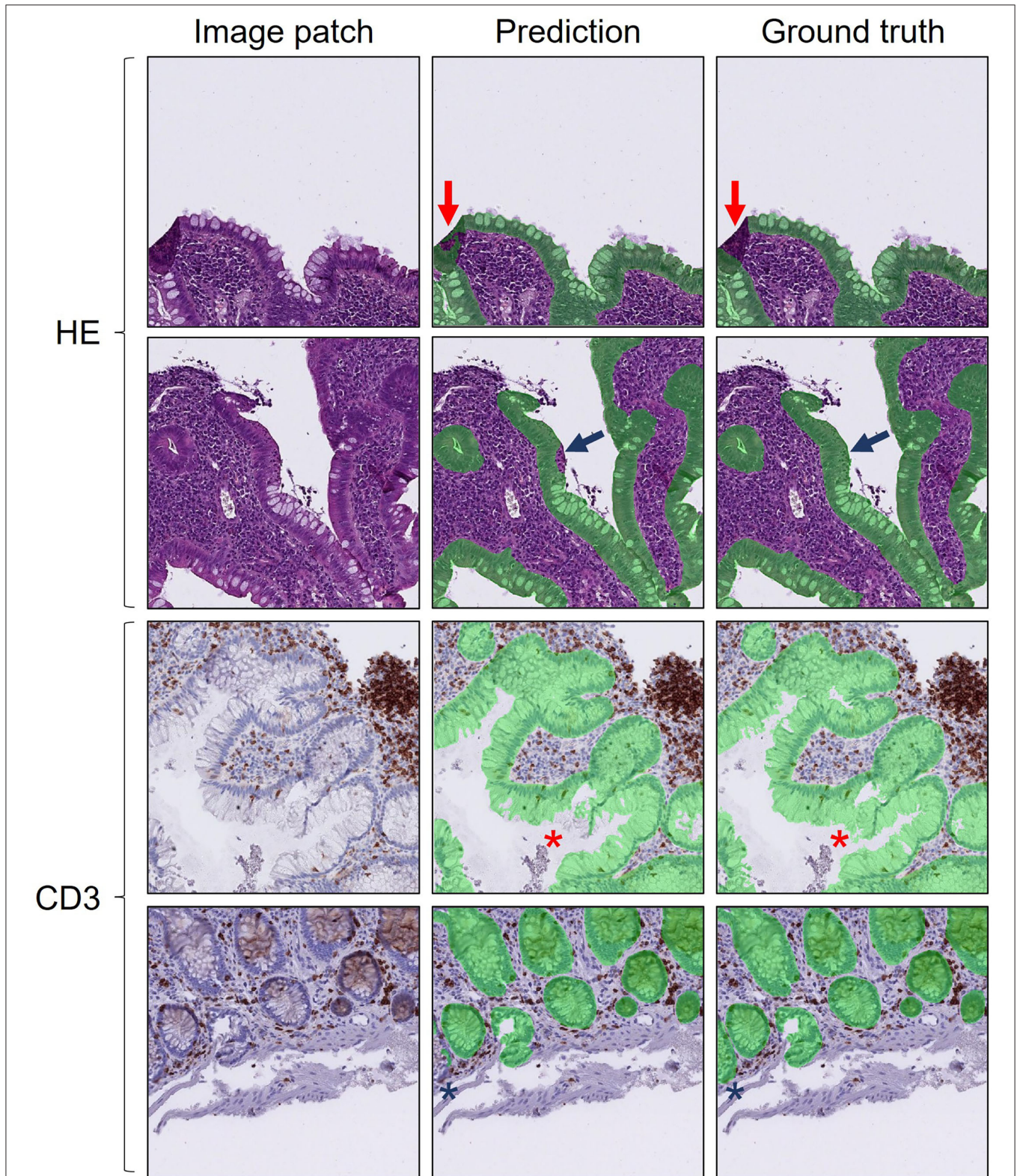
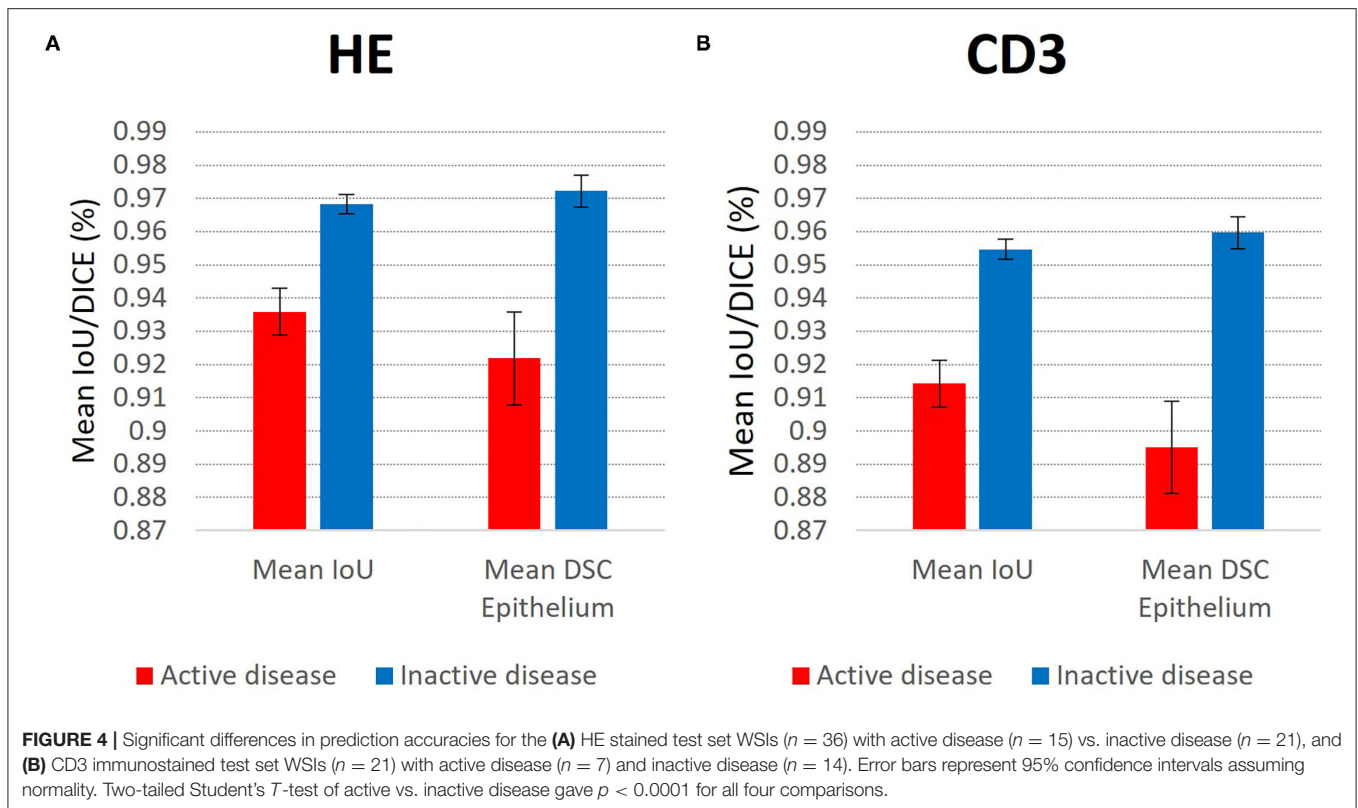


**FIGURE 3 |** Examples of prediction errors in difficult regions: HE stained images with folding artifacts (top row, red arrows) and granuloocyte aggregates (second row, blue arrows). CD3 immunostained images with thick mucin rich epithelium (third row, red stars) and poorly fixated blurred epithelium at the edge of a patch (bottom row, blue stars). Prediction (middle column) and ground truth (right column) of epithelial segmentation are shown in transparent green. 512 × 512-pixel image patches displayed in DeepMIB.



contain both classes. Therefore, slides with more than ~10–20% artifacts were excluded from the dataset, as they contained large areas not suitable for pathological diagnostics either. Furthermore, defining intraepithelial granulocytes as part of the epithelium or not had to be individually considered, as large abscess like assemblies of granulocytes with little or no visible epithelium can obviously not be considered epithelium.

However, the clinical use of an epithelium segmentation algorithm in colon biopsies would certainly involve quantitative estimates of intraepithelial granulocytes and excluding large granulocytic abscesses during annotation also potentially diminishes the clinical value of the algorithm. Indeed, significant differences in prediction accuracies were seen for the test sets of both HE and CD3 immunostained slides between patients with active disease (with infiltration of neutrophilic granulocytes) and inactive disease (see **Figure 4**). Still, the segmentation accuracy was deemed to be at a clinically acceptable level with Epithelium DSC scores > 91% for all slides.

The cytoplasmic part of colon epithelium has a wide variation in size, particularly because of variation of mucin content. Inconsistencies in the cut-off for when mucin is no longer part of the epithelial cell and starts being part of the exterior class, was an obvious source of deviation between ground truth and predictions (see **Figure 3**). Furthermore, the cut-off between when the lumen of the colonic tubule ceases to be part of the epithelium and starts being part of the exterior class, was problematic. This was alleviated to a certain extent

by taking advantage of the power QuPath has as an annotation tool which allows running a single background thresholder pixel classifier algorithm, subsequently creating several large and small background annotations. These could subsequently be selected by a minimal size cut-off and subtracted from the epithelium annotations consistently for the entire dataset by running QuPath scripts in batch mode. A similar procedure is also possible to perform in DeepMIB using the BWThresholding tool followed by subtraction from all annotations, then a small dilation and subsequent similar erosion to fill small holes. One should be aware that this, however, might introduce merging of nearby annotations. The top row of **Figure 2** (HE segmentation results) provides a visual approximation of the maximal colonic tubule lumen sizes that are accepted as being part of the epithelium class (transparent green) or exterior class.

## CONCLUSION

In this paper, we have presented a code-free pipeline for developing and deploying deep neural network segmentation models for computational pathology. The pipeline uses open, free software and enables the user to build and test state-of-the-art deep learning methods for segmentation of WSIs, without requiring any programming experience. We also demonstrate competitive results on two segmentation tasks with rapid inference of about 5 s for an entire WSI. The WSIs and

annotations are also made publicly available to contribute to the active research within the field.

## DATA AVAILABILITY STATEMENT

The dataset of 251 (HE and CD3-stained) colon biopsy WSIs is made openly available at DataverseNO (<https://doi.org/10.18710/TLA01U>). All source code and a tutorial video can be found in the GitHub repository (<https://github.com/andrepd/NoCodeSeg>).

## ETHICS STATEMENT

The studies involving human participants were reviewed and approved by Central Norway Regional Committee for Medical and Health Research Ethics (reference number 2013/212/REKMidt). Written informed consent was provided by all participants in this study.

## AUTHOR CONTRIBUTIONS

HP, AP, IBe, ER, and IBA: writing of initial draft. ER and IBA: provided data material, identified and selected patients from the biobank. ER: conducted all staining and preparation for scanning and the initial annotations of the slides. HP: iteratively improved annotations using the described QuPath/DeepMIB pipeline and performed all DeepMIB semantic segmentation trainings. AP: performed runtime experiments. AP, ES, and IBe: improved respective software to be better suited for this application. IR and EJ: supervised the structuring of the paper and code development for FastPathology/DeepMIB. MS: performed and interpreted statistical analyses comparing architectures. All authors contributed to reviewing and finalizing the manuscript.

## REFERENCES

- Bulten W, Pinckaers H, van Boven H, Vink R, de Bel T, van Ginneken B, et al. Automated deep-learning system for Gleason grading of prostate cancer using biopsies: a diagnostic study. *Lancet Oncol.* (2020) 21:233–41. doi: 10.1016/S1470-2045(19)30739-9
- Ehteshami Bejnordi B, Veta M, Johannes van Diest P, van Ginneken B, Karssemeijer N, Litjens G, et al. Diagnostic assessment of deep learning algorithms for detection of lymph node metastases in women with breast cancer. *JAMA.* (2017) 318:2199–210. doi: 10.1001/jama.2017.14585
- Jackson SL, Frederick PD, Pepe MS, Nelson HD, Weaver DL, Allison KH, et al. Diagnostic reproducibility: what happens when the same pathologist interprets the same breast biopsy specimen at two points in time? *Ann Surg Oncol.* (2017) 24:1234–41. doi: 10.1245/s10434-016-5695-0
- Melia J, Moseley R, Ball RY, Griffiths DF, Grigor K, Harnden P, et al. A UK-based investigation of inter- and intra-observer reproducibility of Gleason grading of prostatic biopsies. *Histopathology.* (2006) 48:644–54. doi: 10.1111/j.1365-2559.2006.02393.x
- van der Laak J, Litjens G, Ciompi F. Deep learning in histopathology: the path to the clinic. *Nat Med.* (2021) 27:775–84. doi: 10.1038/s41591-021-01343-4
- Jahn SW, Plass M, Moinfar F. Digital Pathology: advantages, limitations and emerging perspectives. *J Clin Med.* (2020) 9:3697. doi: 10.3390/jcm9113697
- Djuric U, Zadeh G, Aldape K, Diamandis P. Precision histology: how deep learning is poised to revitalize histomorphology for personalized cancer care. *NPJ Precis Oncol.* (2017) 1:22. doi: 10.1038/s41698-017-0022-1

## FUNDING

This work was funded by the Research Fund for the Center for Laboratory Medicine, St. Olavs Hospital, Trondheim University Hospital, the Faculty of Medicine and Health Sciences, NTNU, the Cancer Foundation, St. Olavs Hospital, Trondheim University Hospital, and the Liaison Committee between the Central Norway Regional Health Authority and NTNU. IBe and EJ are supported by Biocenter Finland and Academy of Finland (project 1331998). Funding for open access publishing was given by NTNU University Library's Open access publishing fund.

## ACKNOWLEDGMENTS

We would like to acknowledge Peter Bankhead (University of Edinburgh), Melvin Gelbard and the rest of the support team working with QuPath for continual feedback and help with sharing scripts and resolving issues with QuPath. The QuPath-related export/import scripts in the GitHub repository are inspired by their shared scripts. We thank the staff of the Gastrointestinal Endoscopy Unit, Department of Gastroenterology and Hepatology, St. Olavs Hospital, Trondheim University Hospital for support with sample collection, Bjørn Munkvold at Department of Clinical and Molecular Medicine (IKOM), NTNU for technical assistance and the Department of Pathology at St. Olavs Hospital, Trondheim University Hospital for scanning the tissue sections.

## SUPPLEMENTARY MATERIAL

The Supplementary Material for this article can be found online at: <https://www.frontiersin.org/articles/10.3389/fmed.2021.816281/full#supplementary-material>

- Srinidhi CL, Ciga O, Martel AL. Deep neural network models for computational histopathology: a survey. *Med Image Anal.* (2021) 67:101813. doi: 10.1016/j.media.2020.101813
- Lara H, Li ZB, Abels E, Aeffner F, Bui MM, ElGabry EA, et al. Quantitative image analysis for tissue biomarker use: a white paper from the digital pathology association. *Appl Immunohistochem Mol Morphol.* (2021) 29:479–93. doi: 10.1097/PAI.0000000000000930
- Lutnick B, Ginley B, Govind D, McGarry SD, LaViolette PS, Yacoub R, et al. An integrated iterative annotation technique for easing neural network training in medical image analysis. *Nat Mach Intell.* (2019) 1:112–9. doi: 10.1038/s42256-019-0018-3
- Miao R, Toth R, Zhou Y, Madabhushi A, Janowczyk A. *Quick Annotator: An Open-Source Digital Pathology Based Rapid Image Annotation Tool.* arXiv:2101.02183 (2021). Available online at: <https://ui.adsabs.harvard.edu/abs/2021arXiv210102183M> (accessed January 01, 2021).
- von Chamier L, Laine RF, Jukkala J, Spahn C, Krentzel D, Nehme E, et al. Democratizing deep learning for microscopy with ZeroCostDL4Mic. *Nat Commun.* (2021) 12:2276. doi: 10.1038/s41467-021-22518-0
- Bankhead P, Loughrey MB, Fernandez JA, Dombrowski Y, McArt DG, Dunne PD, et al. QuPath: open source software for digital pathology image analysis. *Sci Rep.* (2017) 7:16878. doi: 10.1038/s41598-017-17204-5
- Schmidt U, Weigert M, Broaddus C, Myers G. Cell detection with star-convex polygons. *Medical image computing and computer assisted intervention - Miccai 2018. Pt II.* (2018) 11071:265–73. doi: 10.1007/978-3-030-0934-2\_30

15. Moen E, Bannon D, Kudo T, Graf W, Covert M, Van Valen D. Deep learning for cellular image analysis. *Nat Methods*. (2019) 16:1233–46. doi: 10.1038/s41592-019-0403-1
16. Belevich I, Jokitalo E. DeepMIB: user-friendly and open-source software for training of deep learning network for biological image segmentation. *PLoS Comput Biol*. (2021) 17:e1008374. doi: 10.1371/journal.pcbi.1008374
17. Belevich I, Joensuu M, Kumar D, Vihinen H, Jokitalo E. Microscopy image browser: a platform for segmentation and analysis of multidimensional datasets. *PLoS Biol*. (2016) 14:e1002340. doi: 10.1371/journal.pbio.1002340
18. Ronneberger O, Fischer P, Brox T. U-Net: convolutional networks for biomedical image segmentation. Medical image computing and computer-assisted intervention. *Pt Iii*. (2015) 9351:234–41. doi: 10.1007/978-3-319-24574-4\_28
19. Badrinarayanan V, Kendall A, Cipolla R. SegNet: a deep convolutional encoder-decoder architecture for image segmentation. *IEEE Trans Pattern Anal Mach Intell*. (2017) 39:2481–95. doi: 10.1109/TPAMI.2016.2644615
20. Falk T, Mai D, Bensch R, Cicek O, Abdulkadir A, Marrakchi Y, et al. U-Net: deep learning for cell counting, detection, and morphometry. *Nat Methods*. (2019) 16:351. doi: 10.1038/s41592-019-0356-4
21. Pedersen A, Valla M, Bofin AM, De Frutos JP, Reinertsen I, Smistad E. FastPathology: an open-source platform for deep learning-based research and decision support in digital pathology. *IEEE Access*. (2021) 9:58216–29. doi: 10.1109/ACCESS.2021.3072231
22. Smistad E, Bozorgi M, Lindseth F. FAST: framework for heterogeneous medical image computing and visualization. *Int J Comput Assist Radiol Surg*. (2015) 10:1811–22. doi: 10.1007/s11548-015-1158-5
23. Smistad E, Ostvik A, Pedersen A. High performance neural network inference, streaming, and visualization of medical images using FAST. *IEEE Access*. (2019) 7:136310–21. doi: 10.1109/ACCESS.2019.2942441
24. Abadi M, Agarwal A, Barham P, Brevdo E, Chen Z, Citro C, et al. *TensorFlow: Large-Scale Machine Learning on Heterogeneous Distributed Systems*. arXiv:1603.04467 (2016). Available online at: <https://ui.adsabs.harvard.edu/abs/2016arXiv160304467A> (accessed March 01, 2016).
25. Lutter L, Hoytema van Konijnenburg DP, Brand EC, Oldenburg B, van Wijk F. The elusive case of human intraepithelial T cells in gut homeostasis and inflammation. *Nat Rev Gastroenterol Hepatol*. (2018) 15:637–49. doi: 10.1038/s41575-018-0039-0
26. Olivares-Villagomez D, Van Kaer L. Intestinal intraepithelial lymphocytes: sentinels of the mucosal barrier. *Trends Immunol*. (2018) 39:264–75. doi: 10.1016/j.it.2017.11.003
27. Hu MD, Edelblum KL. Sentinels at the frontline: the role of intraepithelial lymphocytes in inflammatory bowel disease. *Curr Pharmacol Rep*. (2017) 3:321–34. doi: 10.1007/s40495-017-0105-2
28. Pettersen HS, Belevich I, Røyset ES, Smistad E, Jokitalo E, Reinertsen I, et al. *140 HE and 111 CD3-stained colon biopsies of active and inactive inflammatory bowel disease with epithelium annotated: the IBDColEpi dataset Version V1* [Annotated histopathological whole slide images, Annotated histopathological image patches]. DataverseNO (2021).
29. Tao A, Sapra K, Catanzaro B. *Hierarchical Multi-Scale Attention for Semantic Segmentation*. arXiv:2005.10821 (2020). Available online at: <https://ui.adsabs.harvard.edu/abs/2020arXiv200510821T> (accessed May 01, 2020).
30. Yuan Y, Chen X, Chen X, Wang J. *Segmentation Transformer: Object-Contextual Representations for Semantic Segmentation*. arXiv:1909.11065 (2019). Available online at: <https://ui.adsabs.harvard.edu/abs/2019arXiv190911065Y> (accessed September 01, 2019).
31. Isensee F, Jaeger PF, Kohl SAA, Petersen J, Maier-Hein KH. nnU-Net: a self-configuring method for deep learning-based biomedical image segmentation. *Nat Methods*. (2021) 18:203–11. doi: 10.1038/s41592-020-01008-z

**Conflict of Interest:** The authors declare that the research was conducted in the absence of any commercial or financial relationships that could be construed as a potential conflict of interest.

**Publisher's Note:** All claims expressed in this article are solely those of the authors and do not necessarily represent those of their affiliated organizations, or those of the publisher, the editors and the reviewers. Any product that may be evaluated in this article, or claim that may be made by its manufacturer, is not guaranteed or endorsed by the publisher.

Copyright © 2022 Pettersen, Belevich, Røyset, Smistad, Simpson, Jokitalo, Reinertsen, Bakke and Pedersen. This is an open-access article distributed under the terms of the Creative Commons Attribution License (CC BY). The use, distribution or reproduction in other forums is permitted, provided the original author(s) and the copyright owner(s) are credited and that the original publication in this journal is cited, in accordance with accepted academic practice. No use, distribution or reproduction is permitted which does not comply with these terms.